

Winding Inductance and Performance Prediction of a Switched Reluctance Motor with an Exterior-rotor Considering the Magnetic Saturation

Minjie Zhang, Nasir Ali, *Student Member, IEEE*, and Qiang Gao, *Member, IEEE*

Abstract—This paper deals with an analytical method to effectively calculate the inductance of an exterior-rotor switched reluctance motor (SRM), which evaluates the winding inductance of both the active section and the end section, accounting for the influence of core saturation. According to the inductance calculated by the analytical model, the flux linkage table and torque table can be established, and the steady state performance such as phase current, flux linkage, copper loss and core loss can be predicted. Effectiveness of this method is verified by the finite element method as well as by experimental results of a 12/8 SRM prototype.

Index Terms—Analytical approach, Exterior-rotor switched reluctance motor, Magnetic saturation, Inductance

I. INTRODUCTION

SWITCHED reluctance motors (SRM) is an attractive candidate for propulsion in electrified transportation system and other safety-critical applications, mostly due to their low-cost and highly robust structure[1,2,etc]. However, accurate design and analysis of an SRM is far more complicated than its counterparts owing to its non-linear magnetic field, which is reflected by its inductance curves dramatically varying both with rotor position and with excitation current. Hence, the accurate knowledge of inductance curves of an SRM is vital for its performance evaluation as well as for control simulation.

The finite element method (FEM) applied on a 3D model is a very accurate way to calculate the inductance of an SRM, as shown in [3]-[6], etc. However, since it is time-consuming, the FEA is generally used for design validation and optimization.

Analytical derivation of inductance is thus attractive for its advantages such as time-saving, much more economic in computing costs, easier for integration with other design tools. Reference [7] presents an analytical model to calculate the unaligned inductance of SRMs with different pole numbers and rotor diameters.

Manuscript received March 19, 2021; revised June 16, 2021; accepted August 10, 2021. date of publication September 25, 2021; date of current version September 18, 2021.

Minjie Zhang, Nasir Ali and Qiang Gao are all with the Department of Electrical Engineering, Shanghai Jiao Tong University, Shanghai, China (email: gaoqiang@sjtu.edu.cn).

Qiang Gao is also with Key Laboratory of Control of Power Transmission and Conversion, Shanghai Jiao Tong University, Ministry of Education, China, 200240

(Corresponding Author: Qiang Gao)

Digital Object Identifier 10.30941/CESTEMS.2021.00025

Reference [8] presents an analytical method to calculate the nonlinear relationship between flux linkages and phase currents of an SRM in aligned rotor positions. References [9]-[10] presented an analytical method for computing minimum and maximum inductances of an inner-rotor SRM without considering the inductance in the intermediate region. References [11]-[13] calculated the inductance profile to predict the performance of SRM without considering the end winding effects. A model for the end inductance calculation of an inner-rotor SRM was presented in [14]-[15], whose calculation error was large, as the core saturation was ignored when a rotor pole was aligned to a stator tooth.

Reference [16] proposed an analytical technique to evaluate the inductance in the active section of an interior-rotor SRM. The inductance of the active region can be calculated in an arbitrary rotor position. Owing to the neglect of the end region inductance, however, the accuracy of this method is limited. Reference [16] also revealed the relationship between phase currents, torque and inductances of an SRM. The flux waveform in each part of an SRM was analyzed through magnetic circuit analysis in reference [17]. It shows the flux waveform of other parts of the motor can be calculated from the flux waveform of the stator core.

As shown in [7]-[16], currently almost all efforts have been devoted to computing the inductance in the active section of interior-rotor SRMs with varying degrees of accuracy. But in many applications, such as in-wheel motor drives for electric vehicles, it will be much more convenient from the perspective of the whole system design to choose an exterior-rotor motor. However, as far as an exterior-rotor SRM is concerned, due to its non-linear feature in the magnetic field and different magnetic line shapes in the air gap, its phase inductance cannot be computed directly with those methods developed for inner-rotor SRMs. This explains the fact that very rare publications have been reported so far about the design, or specifically the analytical winding inductance evaluation of an exterior-rotor SRM. This challenge becomes more prominent if one considers the fact that many inductance calculation methods for inner-rotor SRMs do not include the inductance in the end section, and even some methods do include it, very often the high magnetic saturation effect, which is common in the normal operation of an SRM, is ignored for ease of non-linear calculation. Since the maximum inductance in the end section can account for up to 30% of the total inductance when stator

pole is unaligned with rotor pole [15], it is extremely critical to accurately compute the inductance in the end section to evaluate SRM's performance.

The total inductance of an exterior-rotor SRM has been calculated and the method was presented in [17] by the authors, where some initial simulation results have been provided. More comprehensive analytical derivation of phase inductance of the SRM is detailed in this manuscript, taking the core saturation into account. Following the inductance computation, such critical variables as current, flux, losses and torque are estimated. Furthermore, a prototype of an exterior-rotor SRM has also been built and its test results are reported in this work.

The remaining paragraphs are presented as follows. In Section II, the analytical method to determine the total inductance of an exterior-rotor SRM considering saturation effect is detailed in Section II. Section III deals with its performance prediction. Sections IV and V detail verification of the inductance and performance estimation based on FEA modeling and prototype tests. Finally, Section VI concludes the work.

II. ANALYTICAL MODELING

The following assumptions are made to ease the analysis[16]:

- (1) The magnetic flux lines are straight or semicircular
- (2) Assuming only one phase is excited
- (3) In the stator and rotor pole the magnetic flux lines are parallel to the polar axis
- (4) In the yoke the magnetic flux line is concentric
- (5) The shaft is non-magnetic

In this paper, the inductances in the active section and in the end section will be calculated separately.

A. Equations

For the purposes of illustration, this sub-section shows the principle of inductance calculation in the active section. The basic criterion is also suitable for the end section. Half of the cross section view of a 12/8 exterior-rotor SRM is shown in Fig.1, and the corresponding definition of structure parameters is listed in Table I. In order to simplify the analysis, the calculation is divided into four parts according to the relative position between a rotor pole and a stator pole:

- (1) Totally unaligned position
- (2) Totally aligned position
- (3) Region 1, i.e., between the completely unaligned position to the initial overlapping position
- (4) Region 2, i.e., from the initial overlapping position to the totally aligned position

In the xOy plane the magnetic flux path at the totally unaligned position and the aligned position obtained by FEM is shown in Fig.2, whereby 8 paths are defined to calculate the inductance in the active section when a rotor pole is totally unaligned with a stator pole, as shown in Fig. 2 (b). The paths from 1 to 8 are those for the active inductance evaluation from completely unaligned position to region 2. It is assumed that there is only one path when the rotor pole is completely aligned with the stator pole, as shown in Fig. 2 (a). The rotor position, θ , in region 1 is defined as:

$$0 < \theta \leq \frac{\pi}{N_r} - \frac{(\beta_s + \beta_r)}{2} \quad (1)$$

and the rotor position in region 2 is

$$\frac{\pi}{N_r} - \frac{(\beta_s + \beta_r)}{2} < \theta \leq \frac{\pi}{N_r} \quad (2)$$

where N_r represents number of rotor poles.

Fig.3 shows the general equivalent magnetic circuit for paths 1-8, obtained by Ampere's circuit and magnetic equivalent circuit theorems. The circuit consists of the reluctances of the air gap, the rotor pole, the rotor yoke, the stator pole and the stator yoke i.e., R_{gk} , $R_{rp k}$, R_{ryk} , R_{spk} and R_{syk} , respectively. The applied magnetic motive force (mmf), F_{lk} , is given by

$$F_{lk} = N_p i \quad (3)$$

where N_p and i are number of turns per pole and the current in each pole respectively. On the other hand, the total magnetic voltage, F_{ik} , for each path is defined as

$$F_{ik} = H_{spk} l_{spk} + H_{rp k} l_{rp k} + H_{syk} l_{syk} + H_{ryk} l_{ryk} + H_{gk} l_{gk} \quad (4)$$

where H_{spk} , $H_{rp k}$, H_{syk} , H_{ryk} and H_{gk} denote the magnetic field intensities in the stator pole, rotor pole, stator yoke, rotor yoke and air gap, and l_{spk} , $l_{rp k}$, l_{syk} , l_{ryk} and l_{gk} represent the average length of flux path k in the stator pole, the rotor pole, the stator yoke, the rotor yoke and the air gap.

TABLE I
DEFINITION OF PARAMETER IN FIG. 1

Parameters	Definition	Parameters	Definition
D_r	rotor outer diameter	h_s	stator pole height
D_{ri}	rotor inner diameter	b_{ry}	rotor back iron thickness
D_s	stator outer diameter	b_{sy}	stator back iron thickness
D_{si}	stator inner diameter	β_r	rotor pole arc
h_r	rotor pole height	β_s	stator pole arc

Then the reluctance of the stator pole can be expressed by

$$R_{spk} = \frac{H_{spk} l_{spk}}{B_{spk} A_{spk}} \quad (5)$$

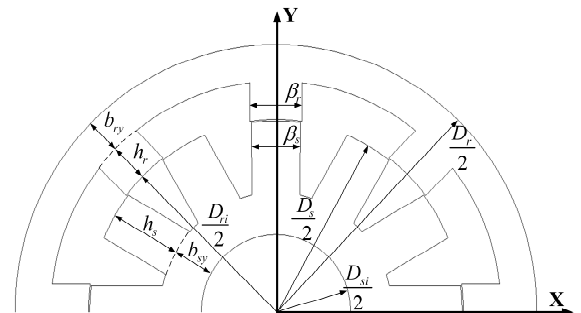


Fig. 1. Cross section view of a 12/8 exterior-rotor SRM.

where B_{spk} represents the flux density in the stator pole of path k , A_{spk} is the mean area of the cross section of the stator pole. During the calculation process of inductance, B_{spk} at any given pole current, i , and rotor position, θ , is stored in a table which is called flux density look-up table in the following sections. The magnetic reluctance of other parts can be obtained similarly.

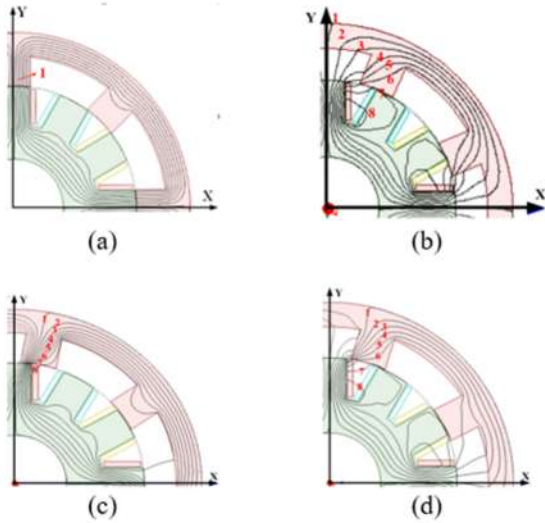


Fig. 2. Magnetic flux distribution in the $x0y$ plane, (a) at the totally aligned position, (b) at the totally unaligned position, (c) region 1, (d) region 2

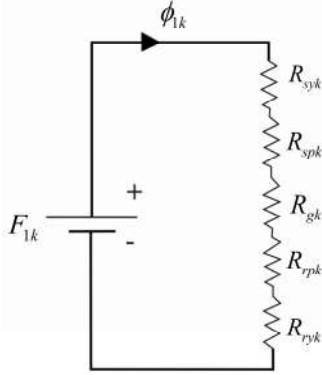


Fig. 3. General equivalent magnetic circuit of paths 1~8

The flux densities of rotor pole, stator yoke, rotor yoke and air gap in the path k ($k=1\sim 8$), can be obtained, respectively, by iterative adjustment of the stator pole flux density, B_{spk} . The magnetic field intensities of each part are then acquired according to the B-H curve. By applying (5) to all the sections in each path, the reluctance of each section can be calculated. The inductance, $L_k(i, \theta)$ can thus be given by

$$L_k(i, \theta) = \frac{4N_p^2}{R_{spk} + R_{rpk} + R_{gk} + R_{syk} + R_{ryk}} \quad (6)$$

The active section total inductance is derived as follows:

$$L_a(i, \theta) = \sum_{k=1}^8 L_k(i, \theta) = \frac{N_p}{i} \sum_{k=1}^8 \phi_k(i, \theta) \quad (7)$$

where ϕ_k represents the magnetic flux in the path k .

B. Inductance in the Active Section

1) Totally Unaligned Position

In the practical control of an SRM, the totally unaligned position of stator and rotor poles is normally defined as $\theta=0^\circ$, as shown in Fig.4.

In order to illustrate the calculation process, the calculation of air gap reluctance in flux path 1 will be given in the following. As shown in Fig.2(a), the flux path 1 is assumed to cross the air gap, split in the rotor yoke, and then re-cross the air gap to the stator pole.

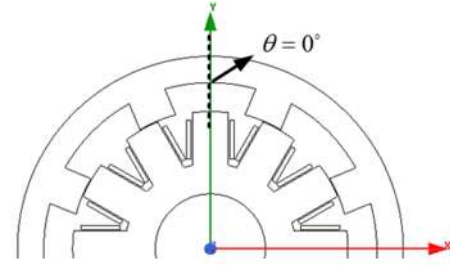


Fig.4. Totally unaligned position of stator and rotor pole

The area of cross section of flux path 1 in the stator pole, air gap and rotor yoke is defined as A_{sp1} , A_{g1} , and A_{ry1} , respectively. And the length of flux path 1 in the stator pole and air gap is defined as l_{sp1} and l_{g1} . According to the actual magnetic line shown in Fig.2, the cross sectional area of flux path 1 in the stator pole is assumed to be 1/4 of stator pole area, therefore

$$A_{sp1} = \frac{1}{4} \times \frac{\beta_s D_s L}{2} = \frac{\beta_s D_s L}{8} \quad (8)$$

where L is the stator iron stack length. The constants in all formula in this paper are set based on the flux distribution in Fig.2.

The length of flux path 1 in the stator pole is assumed to be equal to the stator pole height, therefore

$$l_{sp1} = h_s \quad (9)$$

And the cross sectional area of flux path 1 in the rotor yoke is assumed to be 1/3 of the inner side of rotor yoke area, therefore

$$A_{ry1} = \frac{1}{3} \times \left(\frac{\pi}{4} - \beta_r \right) \left(\frac{D_r}{2} - b_{ry} \right) L \quad (10)$$

When calculating the air gap reluctance, the cross sectional area of flux path 1 in the air gap is assume to be the average of both cross sectional area of rotor yoke, A_{ry1} , and stator pole, A_{sp1} , therefore

$$A_{g1} = \frac{1}{2} (A_{ry1} + A_{sp1}) \quad (11)$$

$$l_{g1} = h_r \quad (12)$$

$$R_{g1} = \frac{l_{g1}}{\mu_0 A_{g1}} \quad (11)$$

And (13) can be further written as

$$R_{g1} = \frac{48h_r}{\mu_0 [3\beta_s D_s + (\pi - 4\beta_r)(D_r - 2b_{ry})]} L \quad (12)$$

At the totally unaligned position, similarly, based on the above assumptions, the air gap reluctance in the flux path k ($k=2\sim 8$), R_{gk} , is given by

$$R_{g2} = \frac{\pi}{12\mu_0 A_{g2}} \left\{ \left[(D_r - 2b_{ry}) \sin \left(\frac{\pi}{24} - \frac{\beta_r}{6} \right) - D_s \sin \frac{\beta_s}{8} \right]^2 + \left[(D_r - 2b_{ry}) \cos \left(\frac{\pi}{24} - \frac{\beta_r}{6} \right) - D_s \cos \frac{\beta_s}{8} \right]^2 \right\}^{1/2} \quad (13)$$

where $A_{g2} = \frac{1}{2} \left(\frac{\beta_s D_s L}{16} + \frac{L}{6} \left(\frac{\pi}{4} - \beta_r \right) \left(\frac{D_r}{2} - b_{ry} \right) \right)$ represents

the mean cross section of air gap for path 2.

$$R_{g3} = \frac{\pi}{12\mu_0 A_{g2}} \left\{ \left[\left(D_r - 2b_{ry} \right) \sin \left(\frac{\pi}{12} - \frac{\beta_r}{3} \right) - D_s \sin \frac{\beta_s}{4} \right]^2 + \left[\left(D_r - 2b_{ry} \right) \cos \left(\frac{\pi}{12} - \frac{\beta_r}{3} \right) - D_s \cos \frac{\beta_s}{4} \right]^2 \right\}^{1/2} \quad (14)$$

$$R_{g4} = \frac{\pi}{18\mu_0 A_{g4}} \left\{ \left[\left(3D_{ri} + 2h_r \right) \sin \theta_1 - 3D_s \sin \frac{3}{8} \beta_s \right]^2 + \left[\left(3D_{ri} + 2h_r \right) \cos \theta_1 - 3D_s \cos \frac{3}{8} \beta_s \right]^2 \right\}^{1/2} \quad (15)$$

$$\text{where } \theta_1 = \frac{\pi}{N_r} - \frac{3D_{ri}\beta_r}{6D_{ri} + 4h_r}, \quad A_{g4} = \frac{1}{2} \left(\frac{\beta_s D_s L}{16} + \frac{2h_r L}{5} \right).$$

$$R_{g5} = \frac{\pi}{6\mu_0 A_{g5}} \left\{ \left[\left(D_{ri} + \frac{7}{32} h_r \right) \sin \theta_2 - \left(D_s - \frac{h_s}{10} \right) \sin \theta_3 \right]^2 + \left[\left(D_{ri} + \frac{7}{32} h_r \right) \cos \theta_2 - \left(D_s - \frac{h_s}{10} \right) \cos \theta_3 \right]^2 \right\}^{1/2} \quad (16)$$

$$\text{where } \theta_2 = \frac{\pi}{N_r} - \frac{\beta_r D_{ri}}{2(D_{ri} + h_r/10)}, \quad \theta_3 = \frac{\beta_s D_s}{2(D_s - 7h_s/32)},$$

$$A_{g5} = \frac{1}{2} \left(\frac{h_s L}{10} + \frac{6}{25} h_r L \right).$$

$$R_{g6} = \frac{\pi}{6\mu_0 A_{g6}} \left\{ \left[D_{ri} \sin \left(\frac{\pi}{N_r} - \frac{39}{80} \beta_r \right) - \left(D_s - \frac{h_s}{4} \right) \sin \theta_4 \right]^2 + \left[D_{ri} \cos \left(\frac{\pi}{N_r} - \frac{39}{80} \beta_r \right) - \left(D_s - \frac{h_s}{4} \right) \cos \theta_4 \right]^2 \right\}^{1/2} \quad (17)$$

$$\text{where } \theta_4 = \frac{\beta_s D_s}{2(D_s - h_s/4)}, \quad A_{g6} = \frac{1}{2} \left(\frac{3}{16} h_s L + \frac{\beta_r D_{ri} L}{15} \right).$$

For paths 7 and 8, the air gap reluctance is obtained by

$$R_{gk} = \frac{k_e (D_s - 2h_s)}{\mu_0 h_s L} \left[\frac{2\pi}{N_s} - \frac{\beta_s D_s}{(D_s - h_s)} \right] \quad (18)$$

where $k_e = 8/3$ for path 7 and $k_e = 4/5$ for path 8.

2) Totally Aligned Position

As shown in Fig. 2(b), only one type of flux path is considered at the totally aligned position, and the air gap reluctance can be defined as:

$$R_g = \frac{l_g}{A_g \mu_0} = \frac{2g}{\mu_0 (\beta_s D_s + \beta_r D_{ri}) L} \quad (19)$$

where g is the air gap length when rotor pole aligned with stator pole.

The reluctances of air gap in region 1 and region 2 can be derived in a similar manner, and the results are given in the

appendices.

C. Inductance in the End Section

The inductance of the end region is heavily influenced by the rotor position and excitation [14]. The end winding inductance at the totally unaligned position slightly increases with an increased excitation. However, when the rotor pole moves into the aligned position of the exciting pole, it decreases with the increase of excitation, as a result of high reluctance path due to core saturation.

Fig. 5 shows the magnetic flux path of the SRM in the yOz plane obtained through a 3D FEM in the totally unaligned position, according to which, the model for inductance calculation in the end section is plotted in Fig. 6. Its equivalent magnetic circuit is similar to that in Fig. 3, except for the air gap reluctance.

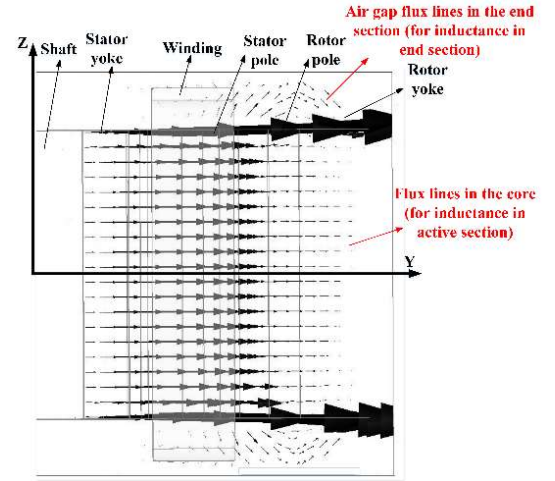


Fig. 5. Magnetic flux path in the yOz plane at the totally unaligned position

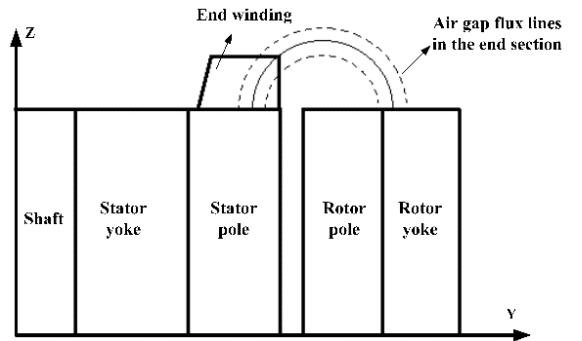


Fig. 6. Model for inductance in the end section at the totally unaligned position

Since total inductance is the sum of inductance in both active section and end section, for convenience in analysis, the flux path in the end section is treated as a semicircle, as shown in Fig. 5. As shown in Fig. 2(a), three kinds of air gap flux path exist:

- (1) Flux path from the stator pole arc to the rotor yoke, like paths 1~3
- (2) Flux path from the stator pole arc to the rotor pole side, like paths 4 and 5
- (3) Flux path from the stator pole side to the rotor pole arc, like paths 6 and 7

Similarly, it is assumed that there are three types of air gap

flux path in the end section defined as paths 9~11. Paths 9~11 are semicircles on yOz plane and take the average length of air gap for these three kinds of flux path in xOy plane as the diameter, respectively. For the path m ($m=9\sim 11$), the air gap reluctance in the end section, $R_{gm}(i, \theta)$, can be obtained by

$$R_{g9} = \begin{cases} \frac{2\pi h_r}{\mu_0 \beta_s D_s h_s}, \theta = 0 \\ \frac{48\pi h_r}{\mu_0 [3\beta_s D_s h_s + (\pi - 4\beta_r)(D_r - 2b_{ry})b_{ry}]}, 0 < \theta \leq \frac{\beta_s}{5} \\ \frac{4\pi}{3\mu_0 [\beta_s D_s h_s + \beta_r D_{ri} h_r]} \left\{ \left[D_s \sin \theta_5 - (D_{ri} + 2h_{r1}) \sin \theta_y \right]^2 \right. \\ \left. + \left[D_s \cos \theta_5 - (D_{ri} + 2h_{r1}) \cos \theta_y \right]^2 \right\}^{1/2}, \frac{\beta_s}{5} < \theta \leq \theta_x \\ \frac{4\pi g}{(\beta_s + \theta_x - \theta) D_s h_s}, \theta_x < \theta \leq \frac{\pi}{N_r} \end{cases} \quad (20)$$

$$\text{where } \theta_x = \frac{\pi}{N_r} - \frac{(\beta_s + \beta_r)}{2}, \theta_y = \frac{\theta_{rp}}{2} - \frac{\beta_r}{2} - \theta, \theta_5 = \frac{7\beta_s}{16\theta_x},$$

$$h_{r1} = \frac{h_r}{\beta_s - 3\theta_x}(\theta - \theta_x)$$

$$R_{g10} = \begin{cases} \frac{\pi}{9\mu_0 \beta_s D_s h_s} \left\{ \left[(3D_{ri} + 2h_r) \sin \theta_6 - 3D_s \sin \frac{3}{8}\beta_s \right]^2 \right. \\ \left. + \left[(3D_{ri} + 2h_r) \cos \theta_6 - 3D_s \cos \frac{3}{8}\beta_s \right]^2 \right\}^{1/2}, \theta = 0 \\ \frac{4\pi}{\mu_0 [\beta_s D_s h_s + (\pi - 4\beta_r)(D_r - 2b_{ry})b_{ry}]} \\ \times \left\{ \left[(D_s - 2h_{s2}) \sin(\beta_s/2) \right. \right. \\ \left. \left. - (D_{ri} + 2h_{r2}) \sin \theta_y \right]^2 - \left[(D_{ri} + 2h_{r2}) \sin \theta_y \right. \right. \\ \left. \left. - (D_{ri} + 2h_{r2}) \cos \theta_y \right]^2 \right\}^{1/2}, 0 < \theta \leq \frac{1}{3}\beta_s \\ \frac{8\pi}{3\mu_0 (\beta_r D_{ri} h_r + \beta_s D_s h_s)} \left\{ \left[(D_s - 2h_{s2}) \sin(\beta_s/2) \right. \right. \\ \left. \left. - D_{ri} \sin \theta_7 \right]^2 + \left[(D_s - 2h_{s2}) \cos(\beta_s/2) \right. \right. \\ \left. \left. - D_{ri} \cos \theta_7 \right]^2 \right\}^{1/2}, \frac{1}{3}\beta_s < \theta \leq \theta_x \\ \frac{10\pi}{\mu_0 (\beta_r D_{ri} h_r + \beta_s D_s h_s)} \left\{ \left[(D_s - 2h_{s3}) \sin\left(\frac{\beta_s}{2}\right) \right. \right. \\ \left. \left. - D_{ri} \sin \theta_8 \right]^2 + \left[(D_s - 2h_{s3}) \cos\left(\frac{\beta_s}{2}\right) \right. \right. \\ \left. \left. - D_{ri} \cos \theta_8 \right]^2 \right\}^{1/2}, \theta_x < \theta \leq \frac{3}{5}\beta_s \\ \frac{4\pi g}{(\beta_s + \theta_x - \theta) D_s h_s}, \frac{3}{5}\beta_s < \theta \leq \frac{\pi}{N_r} \end{cases} \quad (21)$$

$$R_{g11} = \begin{cases} \frac{10\pi}{3\mu_0 (\beta_r D_{ri} h_r + \beta_s D_s h_s)} \left\{ \left[D_{ri} \sin\left(\frac{\pi}{N_r} - \frac{39}{80}\beta_r\right) \right. \right. \\ \left. \left. - \left(D_s - \frac{h_s}{4} \right) \sin \theta_{10} \right]^2 + \left[D_{ri} \cos\left(\frac{\pi}{N_r} - \frac{39}{80}\beta_r\right) \right. \right. \\ \left. \left. - \left(D_s - \frac{h_s}{4} \right) \cos \theta_{10} \right]^2 \right\}^{1/2}, \theta = 0 \\ \frac{16\pi}{3(4\beta_s h_s D_s + \beta_r h_r D_{ri})} \left\{ \left[\left(D_s - \frac{h_s}{3} \right) \sin\left(\frac{\beta_s}{2}\right) \right. \right. \\ \left. \left. - D_{ri} \sin \theta_{10} \right]^2 + \left[\left(D_s - \frac{h_s}{3} \right) \cos\left(\frac{\beta_s}{2}\right) \right. \right. \\ \left. \left. - D_{ri} \cos \theta_{10} \right]^2 \right\}^{1/2}, 0 < \theta \leq \theta_x \\ \frac{16\pi}{3(2\beta_s h_s D_s + \beta_r h_r D_{ri})} \left\{ \left[(D_s - 2h_{s4}) \sin\left(\frac{\beta_s}{2}\right) \right. \right. \\ \left. \left. - D_{ri} \sin \theta_{11} \right]^2 + \left[(D_s - 2h_{s4}) \cos\left(\frac{\beta_s}{2}\right) \right. \right. \\ \left. \left. - D_{ri} \cos \theta_{11} \right]^2 \right\}^{1/2}, \theta_x < \theta \leq \frac{4}{5}\beta_s \\ \frac{4\pi g}{(\beta_s + \theta_x - \theta) D_s h_s}, \frac{4}{5}\beta_s < \theta \leq \frac{\pi}{N_r} \end{cases} \quad (22)$$

$$\text{where } \theta_6 = \frac{\pi}{N_r} - \frac{3D_{ri}\beta_r}{6D_{ri} + 4h_r}, \quad h_{s2} = \frac{h_s}{120}\theta - \frac{h_s}{120},$$

$$h_{r2} = -\frac{h_r}{16}\theta + \frac{5}{16}h_r, \quad \theta_7 = \theta_y + \frac{\beta_r}{30}\theta - \frac{\beta_r}{6}, \quad h_{s3} = -\frac{h_s}{40}\theta - \frac{9}{40}h_s,$$

$$\theta_8 = \theta_y + \frac{\beta_r}{11}, \quad \theta_9 = \frac{\beta_s D_s}{2(D_s - h_s/4)}, \quad \theta_{10} = \theta_y + \frac{1}{45}\beta_r\theta + \frac{2}{45}\beta_r,$$

$$h_{s4} = -\frac{h_s}{30}\theta + \frac{1}{3}h_s, \quad \theta_{11} = \theta_y + \frac{1}{30}\beta_r\theta - \frac{\beta_r}{15}.$$

The flux density of each segment in the core is expressed as (25) by calculating the inductance in the active section.

$$B_k(i, \theta) = \frac{\phi_k(i, \theta)}{A_k} = \frac{L_k(i, \theta)i}{N_p A_k}, k = 1 \sim 8 \quad (23)$$

where A_k and B_k are cross section area and the flux density for the path k obtained by active inductance respectively.

The main difference between inductance derivation in active section and end section is the calculation for magnetic flux density. If one considers the increase of core reluctance caused by core saturation, the core magnetic flux density for end winding calculation can be defined as

$$B_m(i, \theta) = \frac{\phi_m(i, \theta)}{A_m} + \frac{1}{8} \sum_k B_k(i, \theta), k = 1 \sim 8, m = 9 \sim 11 \quad (24)$$

where Φ_m and A_m are magnetic flux and the cross section area for path m respectively. And the flux density look-up table is updated by the average flux density in the stator pole considering the end effect.

$$B_{sp_avg} = \frac{1}{3} \sum_{m=9}^{11} B_{spm} \quad (25)$$

where B_{spm} denotes the flux density in the stator pole for paths 9~11.

Similar to the active section, through iterative adjustment of flux density in the core, inductance in the end section can be obtained.

III. PERFORMANCE PREDICTION

After the inductance is calculated, the inductance and flux linkage profile can be obtained.

A. Phase Current and Flux Linkage

Since the inductance $L(i_k, \theta)$ is a function of both current and rotor position, the k -th phase current i_k under APC can be obtained by (28) when the turn-on angle θ_{on} and turn-off angle θ_{off} are given.

$$\begin{aligned} U_k &= R_{ph} i_k + \omega \frac{d[L(i_k, \theta) i_k]}{d\theta} \\ &= R_{ph} i_k + \omega i_k \left\{ \frac{\partial L(i_k, \theta)}{\partial i} \right\}_{\theta=const} \frac{di_k}{d\theta} + \\ &\quad \left. \frac{dL(i_k, \theta)}{d\theta} \right\}_{i_k=const} + \omega L \frac{di_k}{d\theta} \end{aligned} \quad (26)$$

where $U_k = U_{dc}$ during magnetization, $U_k = -U_{dc}$ during demagnetization. U_k is the k -th phase voltage, U_{dc} is the dc-linkage voltage, R_{ph} is resistance per phase, ω is motor speed.

Flux linkage is a function of phase current and rotor position. The k -th phase flux linkage is defined as

$$\psi_k(i_k, \theta) = L_k(i_k, \theta) i_k \quad (27)$$

Due to the even symmetry [18] characteristic of the flux linkage curve, the flux linkage table in a complete electrical period can be obtained by

$$\psi_k(i_k, \theta) = \psi_k \left(i_k, \frac{2\pi}{N_r} - \theta \right), 0 \leq \theta < \frac{\pi}{N_r} \quad (28)$$

B. Loss Estimation

After the phase current i_k is obtained, the flux linkage curve can be obtained. At the same time, the copper loss per phase is

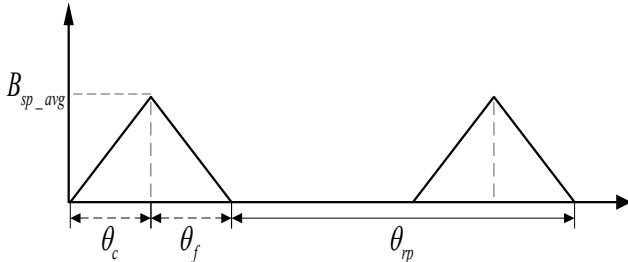


Fig. 7. Flux density waveform in the stator pole

$$P_{cu} = i_k^2 R_{ph} \quad (29)$$

Core loss calculation can be realized with 2D FEM, e.g. [19]-[20], however, core loss prediction in this paper is based on the magnetic circuit analytic method [21]. The flux density waveform of the other parts of the motor can be obtained by calculating the flux waveform of the stator pole. As shown in Fig.7, the flux waveform in the stator pole is assumed to be triangular[14] and its peak value can be obtained by a flux density look-up table stored in the inductance calculation process, where θ_c represents the conduction angle for one phase, and $\theta_c = \theta_{off} - \theta_{on}$, θ_f is the fall angle, θ_{rp} represents the rotor pole pitch, $\theta_{rp} = 2\pi/N_r$. Then, according to the turn-on and turn-off angles, we can calculate the current waveform. According to the current waveform, the peak value of flux density waveform in stator pole is obtained by finding corresponding current at the turn-off angle. Due to the high nonlinearity in the magnetic field of SRM, the flux density waveform contains a large number of high-order harmonic components. Therefore, FFT of flux density in each part of core is conducted by

$$B(t) = \frac{a_0}{2} + \sum_{n=1}^{\infty} [a_n \cos(n\omega_1 t) + b_n \sin(n\omega_1 t)] \quad (32)$$

where a_0 is coefficient of dc component, a_n and b_n are the coefficient of n -th harmonic component, ω_1 is fundamental angular frequency of flux density. The flux density amplitude of fundamental wave and higher harmonics can be expressed as

$$B_k = \sqrt{a_k^2 + b_k^2}, k = 1, 2, \dots, n \quad (33)$$

Core loss calculation in this paper is based on Lavers' model for both hysteresis loss and eddy loss [22]. The eddy loss is expressed as

$$P_e = K_e \sigma_e f^2 B_p^2 \quad (34)$$

where $K_e = \left(\frac{B_1}{B_p} \right)^2 \sum_{i=1}^n \left(\frac{nB_i}{B_1} \right)^2$, B_i is the i -th harmonic

component in the flux density waveform, B_p is the peak value of flux density waveform, σ_e is a constant related to the property of core materials.

The hysteresis loss is expressed as

$$P_h = K_h \sigma_h f B_p^\alpha \quad (35)$$

where

$$K_h = 1 + \frac{k}{B_p} \sum_{i=1}^N \Delta B_i \quad \text{and } 0.6 < k < 0.7, N \text{ is the number of}$$

reversal flux density in the positive half cycle, ΔB_i is the i -th reversal flux density magnitude, σ_h and α are constants related with loss characteristics of the core material.

The friction and windage loss of SRM [21] is

$$P_{fw} = 5.4 \times 10^{-5} n^{0.7} P_N \quad (36)$$

where n is motor speed, P_N is rated power of the SRM.

The stray load loss is calculated as [21]

$$P_s = 0.07(P_{fw} + P_{cu} + P_{fe}) \quad (37)$$

C. Torque Estimation

Since the torque is a function of rotor position and phase

current, torque table can be obtained after the flux linkage profile is calculated. By calculating the co-energy, the instantaneous torque curve at any current and angle be obtained. After flux linkage curve is calculated, the co-energy at any given current and angle is obtained. Then we can get the torque table in the simulation. The relationship between co-energy, W' , and torque is expressed as

$$T(i_k, \theta) = \frac{\partial W'}{\partial \theta} \Big|_{i_k = \text{const}} \quad (38)$$

where $W' = \int_0^{i_k} \psi di$.

Due to the odd symmetry characteristic of the torque curve [18], the torque table in a complete electrical period can be obtained by

$$T(i_k, \theta) = -T\left(i_k, \frac{2\pi}{N_r} - \theta\right), 0 \leq \theta < \frac{\pi}{N_r} \quad (39)$$

IV. SIMULATION VALIDATION

The presented method is employed to predict the total winding inductance of an exterior-rotor SRM. After the total inductance is calculated, the SRM's performance is predicted. Table II lists the main dimensions of this SRM, and Fig.8 shows the 3D FEM model. 35WW250 was selected as the material for the stator and the rotor.

TABLE II
DIMENSIONS OF THE SRM

Parameters	Values
Phases	3
Stator slots	12
Rotor slots	8
Rotor exterior diameter	100.9mm
Stator axial length	40mm
Stator exterior diameter	72mm
Air gap height	0.25mm
Arc coefficient of rotor tooth tip	0.355
Arc coefficient of stator tooth tip	0.5
Series turns per phase	96

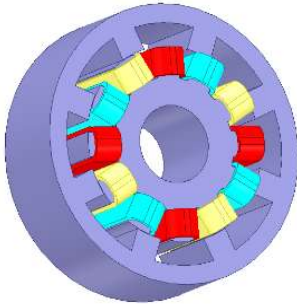


Fig. 8. 3D model of the SRM.

A. Inductance Validation

Fig.9 shows the calculation results of the active section inductance using this method, and they are compared with the

results from the 2D FEM. Since the inductances from 1A to 10A are very close, only those inductances of 1A and 9A are given. The error is smaller than 3%.

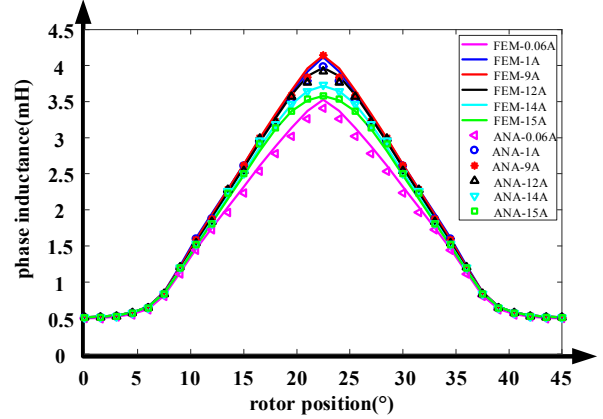
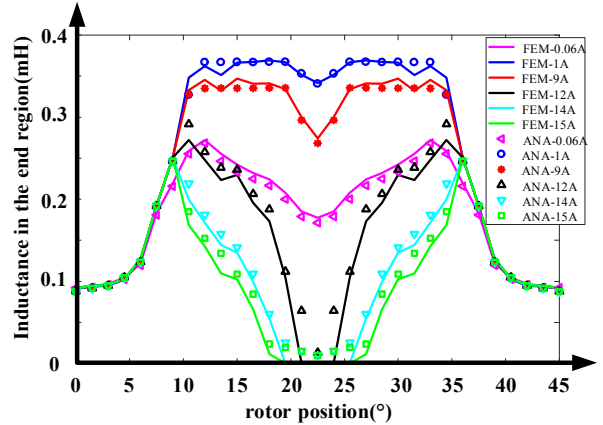
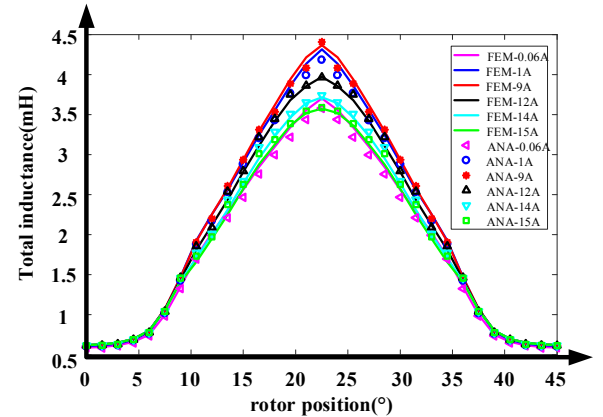


Fig. 9. Comparison of phase active inductance between the presented method (with markers) and 2D FEM (solid lines)

The results of end-winding inductance calculation are given in Fig.10 (a). Except for the extremely saturated region, the error is smaller than 10%, which should be acceptable because the end winding inductance is too small in these saturated regions. As shown in Fig.10(b), the total inductance agrees with the 3D FEA results, and the difference is smaller than 4%.



(a) Inductance in the end region



(b) total inductance

Fig. 10. Comparison of results between the presented method and 3D FEM

B. Loss Estimation and Performance Evaluation

Figs. 11 ~12 show the comparison of the flux linkage table, torque table and flux density table obtained by both analytical model and the 3D FEM, respectively. The error is within 5%.

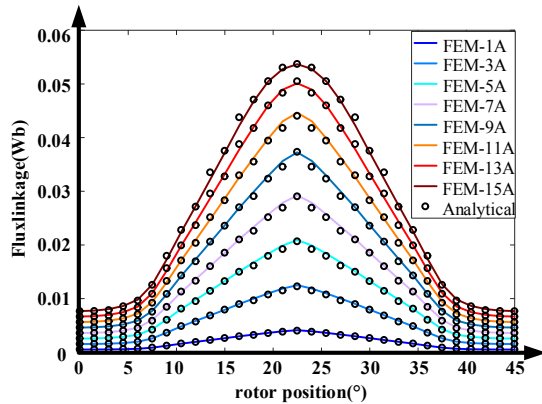


Fig. 11. Comparison of the flux linkage table obtained by the analytical model and the FEM

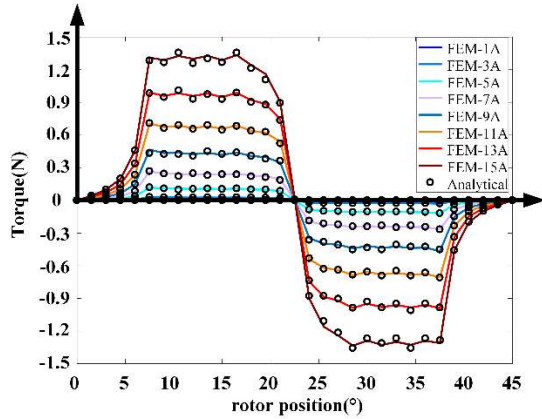


Fig. 12. Comparison of the torque table obtained by the analytical model and the FEM

V. EXPERIMENTAL VALIDATION

An SRM prototype with an exterior rotor has been built, whose dimensions are given in Table II. Fig. 13 shows its photos before assembling. Fig.15(a) shows the experimental phase current when the speed was 500 r/min and 1000 r/min, θ_{on} was 0° and θ_{off} was 20° with a 0.5 Nm torque under APC. Fig.16 (a) shows the phase inductances acquired by the 3D FEM, the proposed method and measurement through a TH2830 LCR meter under no load. The results from the analytical method are aligned with the experimental results, and the error is smaller than 6%, which could be attributed to the difference in permeabilities of the materials in simulation and in the prototype, and also to the machining tolerance.

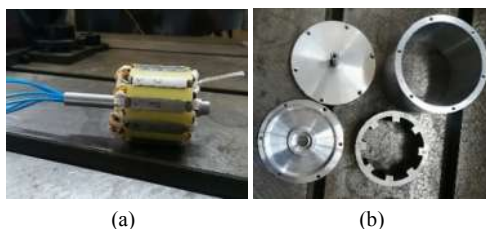


Fig. 13. Photos of the prototype (a), Stator core and windings, (b) Rotor core, frame and covers



Fig. 14. Photo of the experimental platform

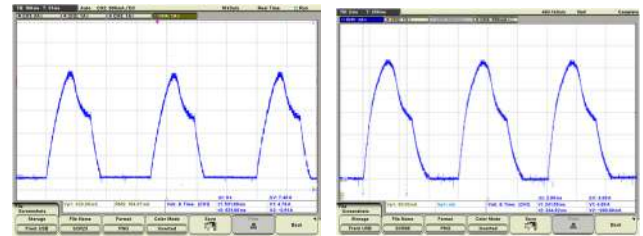


Fig. 15. (a) Current obtained by the experiment with 0.5 Nm, 500 rpm, (b) Current obtained by the experiment with 0.5 Nm, 1000 rpm

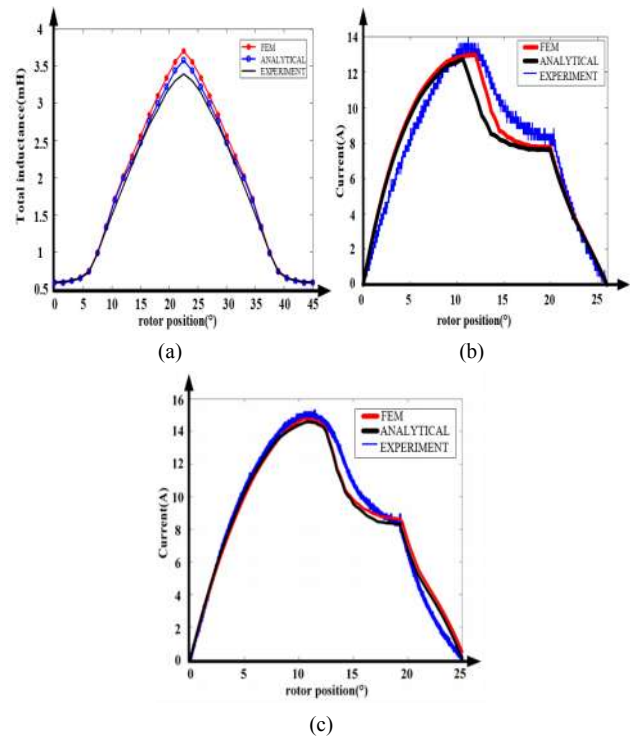


Fig. 16. (a) Inductance curves obtained by the analytical method, FEM and experiment under no load, (b) Current obtained by the experiment, the FEM and the analytical model with 0.5 Nm, 500 rpm, (c) Current obtained by the experiment, the FEM and the analytical model with 0.5 Nm, 1000 rpm

Due to the current limitation of the converter in the test bench, only a maximum torque of 0.5 Nm (about half the rated torque) could be applied. Fig. 16 (b)(c) shows the comparison of phase current obtained by experiment and simulation when the speed was 500 r/min and 1000 r/min, θ_{on} was 0° and θ_{off} was 20° with a 0.5 Nm torque under APC. Table III and Table IV gives the comparison of detailed data calculated by the analytical method and the experiment. It can be seen from the table that the results from the analytical model and the experiment are in good agreement with each other in performance evaluation, with all

the errors well smaller than 10%. It should be pointed out that the efficiency of the motor will increase with the load, which can be seen by the simulation efficiency map shown in Fig.17.

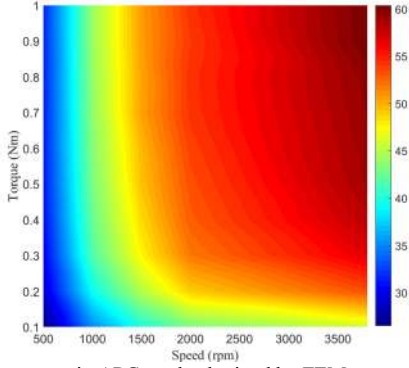


Fig. 17 Efficiency map in APC mode obtained by FEM.

TABLE III

COMPARISON OF RESULTS CALCULATED BY ANALYTICAL METHOD AND FEM (0.5NM, 500RPM)

Parameters	Analytical results	Experiment results	error
Peak current	12.68A	13.89A	-8.7%
Turn-off current	7.88A	8.51A	-7.4%
Average copper loss	60.3W	63.3W	-4.97%
Average core loss	4.28W	4.01W	6.3%
RMSE	-	-	1.33A
Output power	26.18W	26.18W	-
Average torque	0.5Nm	0.5Nm	-
Efficiency	27%	25.8%	4.62%

TABLE IV

COMPARISON OF RESULTS CALCULATED BY ANALYTICAL METHOD AND FEM (0.5NM, 1000RPM)

Parameters	Analytical results	Experiment results	error
Peak current	14.59A	15.03A	-5.1%
Turn-off current	8.34A	8.53A	-2.22%
Average copper loss	74.76W	79.06W	-3.80%
Average core loss	6.42W	6.29W	1.3%
RMSE	-	-	0.4984A
Output power	52.36W	52.36W	-
Average torque	0.5Nm	0.5Nm	-
Efficiency	37.3%	36.2%	3.03%

VI. CONCLUSION

This work presents an analytical method for computing both the active section inductance and end winding inductance for an exterior-rotor SRM. Good agreement of the calculated results by the method with the data from both the finite element analysis and the experiment was achieved. By calculating the inductance of this type of SRMs, such variables as phase current, core loss and copper loss at arbitrary turn-on and turn-off angles under the APC mode can be obtained. Fast optimization of the SRM's performance becomes possible based on this analytical method, combined with an optimum algorithm. It should be pointed out that the prototype SRM was designed and manufactured only for guideline for the design of an exterior-rotor SRM, and as shown in [1] the efficiency of an SRM with much larger power rating for EV or HEV drives is comparable to other candidates.

APPENDIX

A. Inductance in the active section of region 1

In regions 1 and 2, except for path 1, the upper flux path and the lower flux path is asymmetry. Therefore, the reluctance of air gap for path k is divided into upper reluctance, R_{guk} , and lower reluctance, R_{glk} .

$$R_{g1} = \begin{cases} \frac{48h_r}{\mu_0 L} \left[3\beta_s D_s + (\pi - 4\beta_r)(D_r - 2b_{ry}) \right]^{-1}, & 0 < \theta \leq \frac{\beta_s}{5} \\ \frac{8\pi}{3\mu_0 (\beta_s D_s + 2h_r) L} \left\{ \left[D_s \sin \theta_1 - (D_{ri} + 2h_{ru1}) \sin \theta_y \right]^2 + \left[D_s \cos \theta_1 - (D_{ri} + 2h_{ru1}) \cos \theta_y \right]^2 \right\}^{1/2}, & \frac{\beta_s}{5} < \theta \leq \theta_x \end{cases} \quad (A1)$$

$$\text{where } \theta_x = \frac{\pi}{N_r} - \frac{(\beta_s + \beta_r)}{2}, \theta_y = \frac{\theta_{rp}}{2} - \frac{\beta_r}{2} - \theta, \theta_1 = \frac{7\beta_s}{16\theta_x},$$

$$h_{ru1} = \frac{h_r}{\beta_s - 3\theta_x} (\theta - \theta_x).$$

$$R_{gu2} = \begin{cases} \frac{96h_r}{3\mu_0 L} \left[\beta_s D_s + (\pi - 4\beta_r)(D_r - 2b_{ry}) \right]^{-1}, & 0 < \theta \leq \frac{\beta_s}{5} \\ \frac{16\pi}{3\mu_0 (\beta_s D_s + 4h_r) L} \left\{ \left[D_s \sin \theta_2 - (D_{ri} + 2h_{ru2}) \sin \theta_y \right]^2 + \left[D_s \cos \theta_2 - (D_{ri} + 2h_{ru2}) \cos \theta_y \right]^2 \right\}^{1/2}, & \frac{\beta_s}{5} < \theta \leq \theta_x \end{cases} \quad (A2)$$

$$\text{where } h_{ru2} = \frac{29h_r}{64(\beta_s/5 - \theta_x)} (\theta - \theta_x), \theta_2 = \frac{7}{40} \beta_s \theta + \frac{\beta_s}{4}.$$

$$R_{gl2} = \begin{cases} \frac{96h_r}{3\mu_0 \left[\beta_s D_s + (\pi - 4\beta_r)(D_r - 2b_{ry}) \right] L}, & 0 < \theta \leq \frac{\beta_s}{5} \\ \frac{16\pi}{3\mu_0 (\beta_s D_s + 4h_r) L} \left\{ \left[D_s \sin \theta_3 - (D_{ri} + 2h_{rl2}) \sin \theta_y \right]^2 + \left[D_s \cos \theta_3 - (D_{ri} + 2h_{rl2}) \cos \theta_y \right]^2 \right\}^{1/2}, & \frac{\beta_s}{5} < \theta \leq \theta_x \end{cases} \quad (A3)$$

$$\text{where } h_{rl2} = -\frac{h_r}{6} \theta + 3h_r, \theta_3 = \frac{1}{10} \beta_s \theta - \frac{3}{10} \beta_s.$$

$$R_{gu3} = \begin{cases} \frac{8\pi}{3\mu_0 [4h_r + \beta_s D_s] L} \left\{ \left[D_s \sin \theta_4 - (D_{ri} + 2h_{ru3}) \sin \theta_y \right]^2 + \left[D_s \cos \theta_4 - (D_{ri} + 2h_{ru3}) \cos \theta_y \right]^2 \right\}^{1/2}, & 0 < \theta \leq \frac{2}{5} \beta_s \\ \frac{32\pi}{3\mu_0 (\beta_r D_{ri} + 8h_s) L} \left\{ \left[\left(D_s - \frac{h_s}{36} \right) \sin \left(\frac{\beta_s}{2} \right) - D_{ri} \sin \theta_5 \right]^2 + \left[\left(D_s - \frac{h_s}{36} \right) \cos \left(\frac{\beta_s}{2} \right) - D_{ri} \cos \theta_5 \right]^2 \right\}^{1/2}, & \frac{2}{5} \beta_s < \theta \leq \theta_x \end{cases} \quad (A4)$$

$$\text{where } h_{ru3} = -\frac{h_r}{8} \theta + \frac{3h_r}{4}, \theta_4 = \frac{\beta_s}{4} \theta + \frac{\beta_s}{4},$$

$$\theta_5 = \frac{\theta_{rp}}{2} - \frac{7}{10} \beta_r - \theta + \frac{\beta_r}{30} \theta.$$

$$R_{gl3} = \frac{48\pi}{3\mu_0(3\beta_s D_s + 2(\pi - 4\beta_r)(D_r - 2b_{ry}))} L \times \left\{ \left[D_s \sin \theta_6 - (D_r - 2b_{ry}) \sin \theta_7 \right]^2 + \left[D_s \cos \theta_6 - (D_r - 2b_{ry}) \cos \theta_7 \right]^2 \right\}^{1/2} \quad (A5)$$

$$\text{where } \theta_6 = \frac{\beta_s}{12} \theta - \frac{\beta_s}{4}, \theta_7 = \frac{1}{3} \left(\frac{\pi}{4} - \beta_r \right) \left(\frac{\theta}{2} - 1 \right).$$

$$R_{gu4} = \begin{cases} \frac{8\pi}{\mu_0 [6h_s + (\pi - 4\beta_r)(D_r - 2b_{ry})]} L \times \left\{ \left[(D_s - 2h_{su4}) \sin(\beta_s/2) - (D_{ri} + 2h_{ru4}) \sin \theta_y \right]^2 + \left[(D_s - 2h_{su4}) \cos(\beta_s/2) - (D_{ri} + 2h_{ru4}) \cos \theta_y \right]^2 \right\}^{1/2}, & 0 < \theta \leq \frac{1}{3} \beta_s \\ \frac{4\pi}{3\mu_0(h_s + h_r)} L \left\{ \left[(D_s - 2h_{su4}) \sin(\beta_s/2) - D_{ri} \sin \theta_8 \right]^2 + \left[(D_s - 2h_{su4}) \cos(\beta_s/2) - D_{ri} \cos \theta_8 \right]^2 \right\}^{1/2}, & \frac{1}{3} \beta_s < \theta \leq \theta_x \end{cases} \quad (A6)$$

$$\text{where } h_{su4} = \frac{h_s}{120} \theta - \frac{h_s}{120}, h_{ru4} = -\frac{h_r}{16} \theta + \frac{5}{16} h_r,$$

$$\theta_8 = \theta_y + \frac{\beta_r}{30} \theta - \frac{\beta_r}{6}.$$

$$R_{gl4} = \begin{cases} \frac{16\pi}{3\mu_0(\beta_s D_s + 4h_r)} L \left\{ \left[D_s \sin \theta_9 - (D_{ri} + 2h_{rl4}) \sin \theta_z \right]^2 + \left[D_s \cos \theta_9 - (D_{ri} + 2h_{rl4}) \cos \theta_z \right]^2 \right\}^{1/2}, & 0 < \theta \leq \frac{\beta_s}{5} \\ \frac{48\pi}{3\mu_0(3\beta_s D_s + 2(\pi - 4\beta_r)(D_r - 2b_{ry}))} L \times \left\{ \left[D_s \sin \theta_9 - (D_r - 2b_{ry}) \sin \theta_4 \right]^2 + \left[D_s \cos \theta_9 - (D_r - 2b_{ry}) \cos \theta_4 \right]^2 \right\}^{1/2}, & \beta_s/5 < \theta \leq \theta_x \end{cases} \quad (A7)$$

$$\text{where } h_{rl4} = \frac{h_r}{10} (3\theta + 4), \theta_9 = \frac{\beta_r}{12} \theta - \frac{\beta_r}{3}, \theta_z = \frac{\theta_{rp}}{2} - \frac{\beta_r}{2} + \theta,$$

$$\theta_{10} = \frac{1}{8} \left(\frac{\pi}{4} - \beta_r \right) (\theta - 5).$$

$$R_{gu5} = \begin{cases} \frac{4\pi}{3\mu_0(h_s + h_r)} L \left\{ \left[(D_s - 2h_{su5}) \sin(\beta_s/2) - (D_{ri} + 2h_{ru5}) \sin \theta_y \right]^2 + \left[(D_s - 2h_{su5}) \cos(\beta_s/2) - (D_{ri} + 2h_{ru5}) \cos \theta_y \right]^2 \right\}^{1/2}, & 0 < \theta \leq \beta_s/5 \\ \frac{16\pi}{3\mu_0[4h_s + \beta_r D_{ri}]} L \left\{ \left[(D_s - 2h_{su5}) \sin(\beta_s/2) - D_{ri} \sin \theta_{11} \right]^2 + \left[(D_s - 2h_{su5}) \cos(\beta_s/2) - D_{ri} \cos \theta_{11} \right]^2 \right\}^{1/2}, & \beta_s/5 < \theta \leq \theta_x \end{cases} \quad (A8)$$

$$\text{where } h_{su5} = \frac{h_s}{80} \theta + \frac{h_s}{20}, h_{ru5} = -\frac{h_r}{15} \theta + \frac{2}{15} h_r,$$

$$\theta_{11} = \theta_y + \frac{\beta_r}{36} \theta - \frac{\beta_r}{12}.$$

$$R_{gl5} = \begin{cases} \frac{4\pi}{3\mu_0(h_s + h_r)} L \left\{ (D_s - 2h_{sl5}) \sin(-\beta_s/2) \right. \\ \left. (D_{ri} + 2h_{rl5}) \sin \theta_{12} \right]^2 + \left[(D_s - 2h_{sl5}) \cos(-\beta_s/2) \right. \\ \left. - (D_{ri} + 2h_{rl5}) \cos \theta_{12} \right]^2 \right\}^{1/2}, & 0 < \theta \leq \frac{1}{5} \beta_s \\ \frac{48\pi}{3\mu_0[3\beta_s D_s + 2(\pi - 4\beta_r)(D_r - 2b_{ry})]} L \times \left\{ \left[D_s \sin \theta_{13} - (D_r - 2b_{ry}) \sin \theta_4 \right]^2 + \left[D_s \cos \theta_{13} - (D_r - 2b_{ry}) \cos \theta_4 \right]^2 \right\}^{1/2}, & \beta_s/5 < \theta \leq \theta_x \end{cases} \quad (A9)$$

$$\text{where } h_{sl5} = -\frac{h_s}{30} \theta + \frac{h_s}{15}, h_{rl5} = \frac{h_r}{5} \theta, \theta_{12} = -\frac{h_s}{30} \theta + \frac{h_s}{15},$$

$$\theta_{13} = \frac{\beta_s}{12} \theta - \frac{3}{4} \beta_s, \theta_{14} = \left(\frac{\pi}{4} - \beta_r \right) \left(\frac{2}{15} \theta - 1 \right).$$

$$R_{gu6} = \frac{16\pi}{3\mu_0[4h_s + \beta_r D_{ri}]} L \left\{ \left[\left(D_s - \frac{h_s}{3} \right) \sin \left(\frac{\beta_s}{2} \right) - D_{ri} \sin \theta_{15} \right]^2 + \left[\left(D_s - \frac{h_s}{3} \right) \cos \left(\frac{\beta_s}{2} \right) - D_{ri} \cos \theta_{15} \right]^2 \right\}^{1/2} \quad (A10)$$

$$\text{where } \theta_{15} = \theta_y + \frac{1}{45} \beta_r \theta + \frac{2}{45} \beta_r.$$

$$R_{gl6} = \begin{cases} \frac{4\pi}{3\mu_0(h_s + h_r)} L \left\{ (D_s - 2h_{sl6}) \sin(\beta_s/2) \right. \\ \left. (D_{ri} + 2h_{rl6}) \sin \theta_z \right]^2 + \left[(D_s - 2h_{sl6}) \cos(\beta_s/2) \right. \\ \left. - (D_{ri} + 2h_{rl6}) \cos \theta_z \right]^2 \right\}^{1/2}, & 0 < \theta \leq \frac{2}{5} \beta_s \\ \frac{48\pi}{3\mu_0[3\beta_s D_s + 2(\pi - 4\beta_r)(D_r - 2b_{ry})]} L \times \left\{ \left[D_s \sin \theta_{16} - (D_r - 2b_{ry}) \sin \theta_{17} \right]^2 + \left[D_s \cos \theta_{16} - (D_r - 2b_{ry}) \cos \theta_{17} \right]^2 \right\}^{1/2}, & \frac{2}{5} \beta_s < \theta \leq \theta_x \end{cases} \quad (A11)$$

$$\text{where } h_{sl6} = -\frac{h_s}{45} \theta + \frac{2}{15} h_s, h_{rl6} = \frac{h_r}{10} \theta - \frac{h_r}{10}, \theta_{16} = \frac{\beta_s}{10} \theta - \frac{11}{10} \beta_s,$$

$$\theta_{17} = \frac{1}{6} \left(\frac{\pi}{4} - \beta_r \right) (\theta - 9).$$

The air gap reluctance for path 7 and 8 can be obtain by (12).

B. Inductance in the active section of region 2

In region 2, the air gap reluctance is obtained by

$$R_{g1} = \frac{2g}{\mu_0 D_s L \Delta \theta} \quad (A12)$$

where $\Delta\theta = \theta - \theta_x$ being the overlapping angle of rotor and stator pole.

$$R_{gl2} = \begin{cases} \frac{10\pi}{\mu_0(\beta_s D_s + 2h_r)L} \left\{ \left[D_s \sin\left(\frac{2}{5}\beta_s\right) - (D_{ri} + 2h_{rl2}) \sin\theta_y \right]^2 \right. \\ \left. + \left[D_s \cos\left(\frac{2}{5}\beta_s\right) - (D_{ri} + 2h_{rl2}) \cos\theta_y \right]^2 \right\}, \theta_x < \theta \leq \frac{3}{5}\beta_s \\ R_{g1}, \frac{3}{5}\beta_s < \theta < \frac{\pi}{N_r} \end{cases} \quad (A13)$$

where $h_{rl2} = -\frac{h_r}{42}\theta + \frac{9}{42}h_r$.

$$R_{gu4} = \begin{cases} \frac{10\pi}{\mu_0(2h_s + \beta_r D_{ri})L} \left\{ \left[(D_s - 2h_{su4}) \sin\left(\frac{\beta_s}{2}\right) - D_{ri} \sin\theta_{17} \right]^2 \right. \\ \left. + \left[(D_s - 2h_{su4}) \cos\left(\frac{\beta_s}{2}\right) - D_{ri} \cos\theta_{17} \right]^2 \right\}, \theta_x < \theta \leq \frac{3}{5}\beta_s \\ R_{g1}, \frac{3}{5}\beta_s < \theta < \frac{\pi}{N_r} \end{cases} \quad (A14)$$

where $h_{su4} = -\frac{h_s}{40}\theta - \frac{9}{40}h_s$, $\theta_{17} = \theta_y + \frac{\beta_r}{11}$.

$$R_{gl4} = \begin{cases} \frac{10\pi}{\mu_0(\beta_s D_s + 4h_r)L} \left\{ \left[D_s \sin\left(\frac{\beta_s}{4}\right) - (D_{ri} + 2h_{rl4}) \sin\theta_y \right]^2 \right. \\ \left. + \left[D_s \cos\left(\frac{\beta_s}{4}\right) - (D_{ri} + 2h_{rl4}) \cos\theta_y \right]^2 \right\}, \theta_x < \theta \leq \frac{2}{3}\beta_s \\ R_{g1}, \frac{2}{3}\beta_s < \theta < \frac{\pi}{N_r} \end{cases} \quad (A15)$$

where $h_{rl4} = -\frac{h_r}{10}\theta + h_r$.

$$R_{gu5} = \begin{cases} \frac{10\pi}{\mu_0(7h_s + \beta_r D_{ri})L} \left\{ \left[(D_s - 2h_{su5}) \sin\left(\frac{\beta_s}{2}\right) - D_{ri} \sin\theta_{18} \right]^2 \right. \\ \left. + \left[(D_s - 2h_{su5}) \cos\left(\frac{\beta_s}{2}\right) - D_{ri} \cos\theta_{18} \right]^2 \right\}^{1/2}, \theta_x < \theta \leq \frac{2}{3}\beta_s \\ R_{g1}, \frac{2}{3}\beta_s < \theta < \frac{\pi}{N_r} \end{cases} \quad (A16)$$

where $h_{su5} = -\frac{h_s}{25}\theta - \frac{2}{5}h_s$, $\theta_{18} = \theta_y + \frac{\beta_r}{6}$.

$$R_{gl5} = \begin{cases} \frac{28\pi}{3\mu_0(\beta_s D_s + 7h_r)L} \left\{ \left[D_s \sin\left(\frac{\beta_s}{4}\right) - (D_{ri} + 2h_{rl5}) \sin\theta_y \right]^2 \right. \\ \left. + \left[D_s \cos\left(\frac{\beta_s}{4}\right) - (D_{ri} + 2h_{rl5}) \cos\theta_y \right]^2 \right\}^{1/2}, \theta_x < \theta \leq \frac{2}{3}\beta_s \\ R_{g1}, \frac{2}{3}\beta_s < \theta < \frac{\pi}{N_r} \end{cases} \quad (A17)$$

where $h_{rl5} = -\frac{h_r}{4}\theta + \frac{5}{2}h_r$.

$$R_{gu6} = \begin{cases} \frac{16\pi}{3\mu_0(4h_s + \beta_r D_{ri})L} \left\{ \left[(D_s - 2h_{su6}) \sin\left(\frac{\beta_s}{2}\right) - D_{ri} \sin\theta_{19} \right]^2 \right. \\ \left. + \left[(D_s - 2h_{su6}) \cos\left(\frac{\beta_s}{2}\right) - D_{ri} \cos\theta_{19} \right]^2 \right\}^{1/2}, \theta_x < \theta \leq \frac{4}{5}\beta_s \\ R_{g1}, \frac{4}{5}\beta_s < \theta < \frac{\pi}{N_r} \end{cases} \quad (A18)$$

where $h_{su6} = -\frac{h_s}{30}\theta + \frac{1}{3}h_s$, $\theta_{19} = \theta_y + \frac{1}{30}\beta_r\theta - \frac{\beta_r}{15}$.

$$R_{gl6} = \begin{cases} \frac{4\pi}{\mu_0(\beta_s D_s + 3h_r)L} \left\{ \left[D_s \sin\theta_{20} - (D_{ri} + 2h_{rl6}) \sin\theta_y \right]^2 \right. \\ \left. + \left[D_s \cos\theta_{20} - (D_{ri} + 2h_{rl6}) \cos\theta_y \right]^2 \right\}^{1/2}, \theta_x < \theta \leq \frac{4}{5}\beta_s \\ R_{g1}, \frac{4}{5}\beta_s < \theta < \frac{\pi}{N_r} \end{cases} \quad (A19)$$

where $h_{rl6} = -\frac{h_r}{4}\theta + \frac{11}{4}h_r$, $\theta_{20} = \frac{1}{24}\beta_r\theta - \frac{\beta_r}{3}$.

The lower air gap reluctance for path 3 is calculated by (A13), where the h_{rl2} is replaced by h_{rl3} .

$$h_{rl3} = -\frac{h_r}{11}\theta + \frac{9}{11}h_r \quad (A20)$$

In region 2, if the reluctance for air gap is not mentioned above, it equals to R_{g1} .

REFERENCES

- [1] Z. Yang, F. Shang, I.P. Brown, and M. Krishnamurthy, "Comparative Study of Interior Permanent Magnet, Induction, and Switched Reluctance Motor Drives for EV and HEV Applications," *IEEE Transactions on Transportation Electrification*, vol. 1, no. 3, pp. 245-254, 2015.
- [2] A. A. S. Bukhari, B.P. Alalibo, and W.P. Cao, et al., "Switched reluctance motor design for electric vehicles based on harmonics and back EMF analysis," *The Journal of Engineering*, vol. 2019, no. 17, pp. 4220-4225, 2019.
- [3] X. Chen and J. Wu, "Calculation of inductances with 3-D FEM for SRM with segmental rotors and fully-pitched windings," in *Proc. of 17th International Conference on Electrical Machines and Systems (ICEMS)*, Hangzhou, China, 2014, pp. 1822-1824.
- [4] P. N. Kumar and T. B. Isha, "Inductance calculation of 8/6 switched reluctance motor," in *Proc. of International Conference on Power System*

Technology and IEEE Power India Conference, New Delhi, India, 2008, pp. 1-5.

- [5] B.Nguyen and C.Ta, "Finite element analysis, modeling and torque distribution control for switched reluctance motors with high non-linear inductance characteristics," in *Proc. of IEEE International Electric Machines & Drives Conference (IEMDC)*, Niagara Falls, 2011, pp. 693-698.
- [6] Z.Xu, K.I Jeong, D.H. Lee, et al., "Preliminary performance evaluation of a novel 12/8 segmental rotor type SRM," in *Proc. of 19th International Conference on Electrical Machines and Systems (ICEMS)*, China, 2016, pp. 1-5.
- [7] A Radun, "Analytical calculation of the switched reluctance motor's unaligned inductance," *IEEE Transactions On Magnetics*, 1999,35(6), pp.4473-4481.
- [8] B.Schinnerl and D. Gerling, "Novel analytical calculation method for the non-linear ψ -i-characteristic of switched-reluctance-machines in the aligned rotor position," in *Proc. of IEEE International Electric Machines & Drives Conference (IEMDC)*, Antalya, Turkey, 2007, pp. 793-796
- [9] A.Michaelides, C. Pollock and C.Jolliffe, "Analytical computation of minimum and maximum inductances in single and two phase switched reluctance motors," *IEEE Transactions On Magnetics*, vol 2, no 33, pp.2037-2040, 1997.
- [10] S. H.Mao, D. Dorrell and M.C.Tsai, "Fast analytical determination of aligned and unaligned flux linkage in switched reluctance motors based on a magnetic circuit model," *IEEE Transactions On Magnetics*, vol. 45, no. 7, pp. 2935-2942, 2009.
- [11] A. J. P.Ortega, S. Paul, R. Islam, et al, "Analytical Model for Predicting Effects of Manufacturing Variations on Cogging Torque in Surface-Mounted Permanent Magnet Motors," *IEEE Transactions On Industry Applications*, vol. 52, no. 4, pp. 3050-3061, 2016.
- [12] Z.Zhang, S. Rao, and X. P. Zhang, "Performance Prediction of Switched Reluctance Motor using Improved Generalized Regression Neural Networks for Design Optimization," *CES Transactions On Electrical Machines And Systems*, vol. 2, no. 4, pp. 371-376, 2018.
- [13] S. H.Won, J. S. Ahn, K. C. Kim, et al, "Performance Prediction of Switched Reluctance Motor Considering Windage Loss for High Speed Application," in *Proc. of 12th Biennial IEEE Conference on Electromagnetic Field Computation*, Miami, FL, USA,2006 pp.417-417.
- [14] A.Schramm and D. Gerling, "Analytical Calculation of the End Winding Leakage Inductance Based on the Solution of Neumann Integrals," in *Proc. of IEEE ISIE*, 2005, Dubrovnik, Croatia, pp.98-105.
- [15] J. W.Sun, D. X. Bian and X. L. Liang, "Analysis and Calculation on SRM's End-Windings Inductance," *Journal of Shandong University of Technology*, vol. 22, no. 5, pp. 52-55, 2008.
- [16] R. Krishnan, *Switched Reluctance Motor Drives: Modeling, Simulation, Analysis, Design, and Applications*, CRC Press, 2001.
- [17] M. J. Zhang, Q. Gao and X. Cai, "Analytical Inductance Calculation of an Outer Rotor Switched Reluctance Motor," in *Proc.of 22th International Conference on Electrical Machines and Systems (ICEMS)*, 2019, Harbin, China, pp.1-6.
- [18] M. D. Bui and U. Schaefer, "Core Losses Measurement Technique for High Frequency and Flux Density of Switched Reluctance Machines," in *Proc. of International Conference on Electrical Machines*, Marseille, 2012, pp.1619-1624.
- [19] J. F. Pan, F. J. Meng and N. C. Cheung, "Core loss analysis for the planar switched reluctance motor," *IEEE Transactions on Magnetics*, vol. 50, no. 2, pp. 813-816, 2014.
- [20] B. Ganji, J. Faiz, K. Kasper, et al, "Core loss model based on finite-element method for switched reluctance motors," *IET Electric Power Applications*, vol. 4, no. 7, pp.569-577, 2010.
- [21] P.N Materu and R. Krishnan, "Estimation of switched reluctance motor losses," *IEEE Transactions On Industry Applications*, vol. 28, no. 3, pp.668-697, 1992.
- [22] J.D. Lavers, P.P. Biringer and H. Hollitscher, "A Simple Method of Estimating the Minor Loop Hysteresis Loss in Thin Laminations," *IEEE Trans. on Magnetics*, vol. 5, no.14, pp386-388, 1978.



Minjie Zhang was born in Guilin, China in 1993. She received the B.Sc. and M.Sc. degree, in 2015 and 2020 respectively, both in electrical engineering from Shanghai Jiao Tong University (SJTU), Shanghai, China. Since 2020, she has been working as a Research Assistant at SJTU.

Her current research interests include optimal design and control of Permanent Magnet Synchronous Motor (PMSM) and Switched Reluctance Motor (SRM), noise reduction in motor control, and related artificial intelligence algorithms.



Nasir Ali received the B.Sc. degree in electrical engineering from FAST-National University of Computer and Emerging Sciences (FAST-NUCES), Karachi, Pakistan, in 2015, and the M.Sc. degree in electrical engineering from Shanghai Jiao Tong University (SJTU), Shanghai, China, in 2018. He is currently pursuing the Ph.D. degree in electrical engineering at the school of Electronic Information and Electrical engineering (SEIEE), SJTU, Shanghai, China.

His current research interests include fault diagnosis and fault tolerant control of Switched Reluctance Motor (SRM) drives.



Qiang Gao received the B.Sc. and M.Sc. degrees, in 1998 and 2001 respectively, both in electrical engineering from Shanghai Jiao Tong University (SJTU), Shanghai, China, and the Ph.D. degree in 2007 from University of Nottingham (UoN), Nottingham, U.K.

After receiving the M.Sc. degree, from 2001 to 2003, he was a R&D engineer with the Delta Power Electronics Centre, Delta Electronics, Shanghai. From 2006 to 2009, he was with the Department of Electrical and Electronic Engineering, UoN, working as a research fellow on PMSM's sensorless control using matrix converter. In October 2009, he joined the Department of Electrical Engineering and the Wind Power Research Centre of SJTU, and was appointed as an associate professor. His current research interests include electric machines and their control, power converters and wind power generation.